Available online at www.sciencedirect.com

ScienceDirect

Acta Materialia 80 (2014) 478–489

Acta MATERIALIA

www.elsevier.com/locate/actamat

Variant selection and intervariant crystallographic planes distribution in martensite in a Ti–6Al–4V alloy

Hossein Beladi [a,*], Qi Chao [a], Gregory S. Rohrer [b]

[a] Institute for Frontier Materials, Deakin University, Geelong, VIC 3216, Australia
[b] Department of Materials Science and Engineering, Carnegie Mellon University, Pittsburgh, PA 15213-3890, USA

Received 29 May 2014; received in revised form 24 June 2014; accepted 24 June 2014

Abstract

The transformation texture was studied in a Ti–6Al–4V alloy for two microstructures produced through different phase transformation mechanisms (i.e. diffusional vs. displacive). Both microstructures revealed qualitatively similar crystallographic texture characteristics, having two main texture components with Euler angles of (90°, 90°, 0°) and (90°, 30°, 0°). However, the overall α texture strength was considerably weaker in the martensitic structure (i.e. displacive mechanism) compared with the α + β microstructure produced through slow cooling (i.e. diffusional mechanism). The intervariant boundary distribution in martensite mostly revealed five misorientations associated with the Burgers orientation relationship. The five-parameter boundary analysis also showed a very strong interface plane orientation texture, with interfaces terminated mostly on the prismatic planes $\{hki0\}$, when misorientation was ignored. The highest intervariant boundary populations belonged to the 63.26°/$[\overline{1}0\ 5\ 5\ \overline{3}]$ and 60°/$[1\ 1\ \overline{2}\ 0]$ misorientations, with length fractions of 0.38 and 0.3, respectively. The former was terminated on $(4\ \overline{1}\ \overline{3}\ 0)$, and the latter was a symmetric tilt boundary, terminated on $(\overline{1}\ 0\ 1\ 1)$. The intervariant plane distribution in martensite was determined more by the constraints of the phase transformation than by the relative interface energies.

Keywords: Ti–6Al–4V; Martensite; Texture, Intervariant plane distribution, Variant selection; Electron backscatter diffraction

1. Introduction

Phase transformations in metals are the most effective way to tailor their microstructure and properties. The transformations often follow particular relationships between lattice orientations in the parent and daughter (transformed) phases. In titanium and zirconium alloys, the most commonly cited relationship is the Burgers orientation relationship, where the phase transformation takes place between a high-temperature body centered cubic (bcc) phase β, and a low-temperature hexagonal close packed phase α during both cooling (β → α) and heating (α → β) [1]. Here, two parallel planes correspond to both close-packed planes, $(1\ 0\ 1)_\beta \parallel (0\ 0\ 0\ 1)_\alpha$, whereas the two parallel directions relate to the nearest-neighbor directions, $[1\ 1\ \overline{1}]_\beta \parallel [1\ 1\ \overline{2}\ 0]_\alpha$ (Fig. 1) [2]. Therefore, a single β grain can potentially transform to 12 possible orientations/variants during the β → α phase transformation. This should lead to a weak (random) final α texture if all variants are formed with equal statistical probability during the β → α phase transformation.

The texture resulting from diffusional phase transformations in Ti and Zr alloys, however, differs significantly from the theoretical texture expected from the Burgers orientation relationship [3–5]. In other words, diffusional phase transformations lead to the occurrence of specific orientations/variants through a phenomenon known as variant selection. Four possible mechanisms have been linked to

* Corresponding author. Tel.: +61 3 5227 1250, mobile: +61 402 532 477; fax: +61 3 5227 1103.
E-mail address: hossein.beladi@deakin.edu.au (H. Beladi).

http://dx.doi.org/10.1016/j.actamat.2014.06.064
1359-6454/

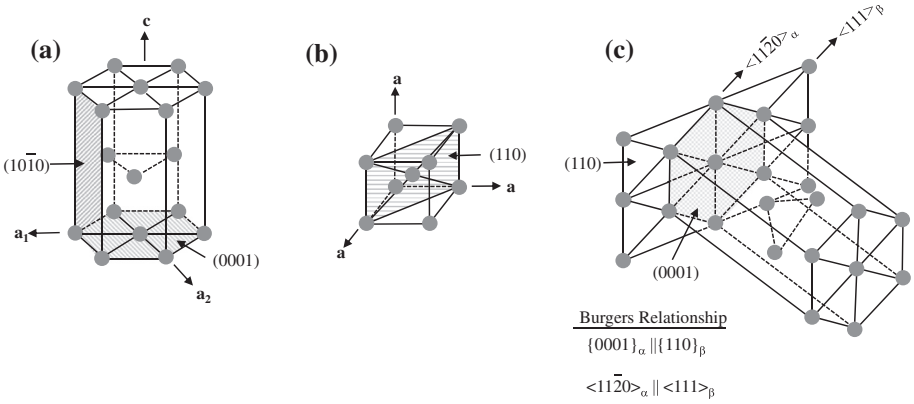

Fig. 1. Schematic representation of (a) hexagonal α phase, (b) bcc β phase and (c) the Burgers orientation relationship between the α and β phases during phase transformation.

variant selection: (i) the retained stress in the high-temperature phase, due to a volume change on heating [4,6] and/or externally applied deformation [7], biases the transformation product characteristics on cooling; (ii) the existence of metastable α at high temperature, which acts as nuclei for growth on cooling [3,8]; (iii) the self-accommodation of the strains produced by the $\beta \rightarrow \alpha$ transformation through the formation of specific variant cluster arrangements [9,10]; and (iv) the presence of specific grain boundary characteristics in the high-temperature β phase, enhancing the nucleation of certain orientations/variants during phase transformation [11–15]. Among the different hypotheses, the latter was considered the best possible reason for the strong variant selection observed during phase transformations for both Ti and Zr alloys. Bhattacharyya et al. [11] were among the first to demonstrate that high-temperature β grain boundaries in Ti have a tendency to terminate on {1 1 0} planes, resulting in the nucleation of α variants with close alignment of their (0 0 0 1) poles on both sides of the β boundary.

The extent of variant selection (texture development) through the $\beta \rightarrow \alpha$ transformation may, however, be influenced by high-temperature β phase characteristics (texture [3,16] and grain size [15]), as well as heat treatment parameters (annealing temperature and cooling rate [3]). Among the different parameters affecting the variant selection mechanism, the effect of cooling rate on the variant selection during the $\beta \rightarrow \alpha$ phase transformation in Ti alloys has received the least attention. For comparison, it is known that the promotion of the displacive phase transformation (increasing cooling rate or undercooling) weakens the variant selection in Zr alloys [3] and steels [17,18]. Therefore, the first objective of this paper is to describe the influence of cooling rate on the variant selection mechanism during the $\beta \rightarrow \alpha$ transformation in a Ti–6Al–4V alloy (i.e. diffusional vs. displacive phase transformation).

Accelerating the cooling rate promotes a displacive phase transformation mechanism, leading to the formation of a martensitic microstructure consisting of laths/plates with a high dislocation density and/or twins, depending on composition [9,10,19]. The crystallography of the $\beta \rightarrow \alpha$ martensitic transformation has been comprehensively studied over the past decades. The core emphasis was given to morphology [10], orientation relationship [19], habit plane [19,20], lath/plate dislocation substructure [10,21] and self-accommodation effects [9,10]. A limited attempt was also made to characterize the intervariant interfaces formed through the martensitic transformation using transmission electron microscopy (TEM), though it was restricted to only one boundary type [9,10]. This is not surprising, as the conventional techniques for the characterization of interface/boundary planes, such as TEM and three-dimensional electron backscatter diffraction (EBSD) techniques, are still relatively complex and time consuming.

Recent developments in characterization techniques make it feasible to statistically measure all five independent boundary parameters (i.e. three lattice misorientations and two plane orientations) in polycrystalline materials with different crystal structures [22–31]. This approach measures all five macroscopic parameters from conventional EBSD maps using automated trace analysis software [32]. Only one five-parameter analysis has been carried out for Ti–6Al–4V alloy so far, and it did not exactly examine the boundaries expected from the Burgers orientation relationship [29]. The second objective of the current work is, therefore, to provide a detailed description of the intervariant interface/boundary character distribution in a martensitic microstructure formed in a Ti–6Al–4V alloy using the five-parameter grain boundary analysis approach. The motivation for this quantitative analysis of the interface distributions is to develop structure–property relationships for this important alloy. Knowledge of the evolution of the grain boundaries and interfaces during phase transformations and their relationship to properties could ultimately be used to control the mechanical properties of the Ti–6Al–4V alloy.

2. Experimental procedure

2.1. Material

The alloy used in the current study had a composition of 6.05Al, 3.98V, 0.12O, 0.092Fe, 0.01N, 0.04C, 0.002H and

balance Ti (in wt.%). The material was received as a hot-rolled plate with a thickness of 5.75 mm, having a microstructure that consisted of α with a plate morphology, delineated by fine β phase films (Fig. 2a). The as-received plate was subjected to two heat treatment conditions: (i) reheating to 1100 °C in an argon atmosphere and annealing for 30 min, followed by ice-water quenching to obtain a fully martensitic microstructure (i.e. α; Fig. 2c, d); and (ii) reheating to 1020 °C in an argon atmosphere and annealing for 30 min, followed by slow cooling, at a rate of 1 °C min^{-1}, resulting in a lamellar α + β microstructure (Fig. 2e, f).

2.2. Microstructural characterization

The microstructures formed from both heat treatment conditions were examined using different characterization techniques, such as optical microscopy (OM), scanning electron microscopy (SEM) equipped with electron backscattered diffraction (EBSD), and X-ray diffraction (XRD). For OM, the specimens were mechanically polished and then etched in Kroll's reagent (i.e. 2% HF, 6% HNO_3 and 92% H_2O). The specimens for SEM, EBSD and XRD characterization were further polished by a colloidal silica slurry solution after standard mechanical polishing.

A field emission Zeiss-SUPRA 55-VP scanning electron microscope integrated with a Zeiss angle selective backscattered (AsB) electron detector was also employed to reveal the microstructure through backscattered imaging at high magnification. This technique provides greater spatial resolution over traditional high-angle collection detectors and enables the observation of detailed microstructural information about features such as subgrains, dislocations and nano-scale mechanical twins [33].

2.3. Texture measurement

Phase identification and texture measurement were performed with a PANalytical X-ray diffractometer using Cu K_α radiation in point focus. The texture measurement was performed on the rolling direction–transverse direction (RD/TD) plane using X-ray diffraction. Owing to a coarse prior β grain structure (i.e. >420 μm) formed through the

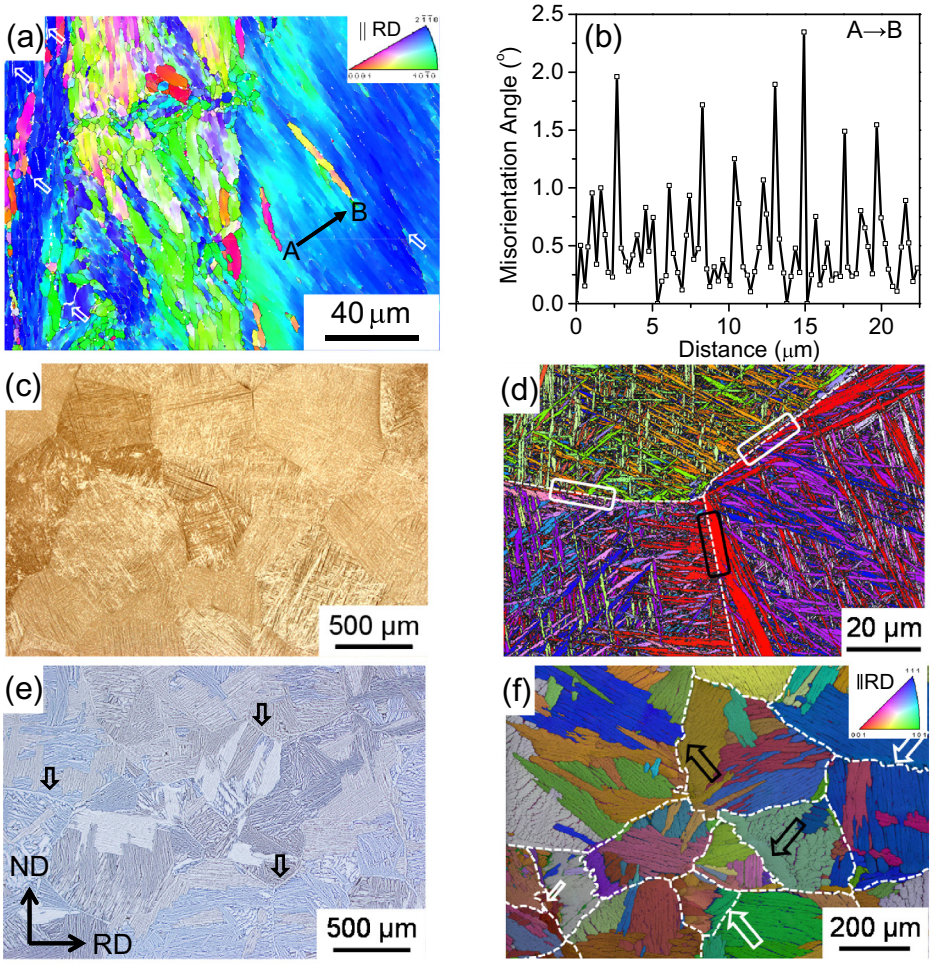

Fig. 2. (a, c–f) Microstructure of Ti–6Al–4V alloy at different heat treatment conditions: (a) as-received (EBSD inverse pole figure (IPF)); (c) martensite (OM); (d) martensite (EBSD IPF); (e) lamellar α + β microstructure (OM); and (f) lamellar α + β microstructure (EBSD IPF). (b) The point to point misorientation angle profile across the α plates (line A → B) in (a). The β phase is indicated by the white arrows in (a). Insets in (a) and (f) represent the color codes for α and β phases, respectively. ND and RD are normal and rolling directions, respectively.

heat treatment schedule of both martensitic and lamellar $\alpha+\beta$ microstructures, a relatively large specimen ($\sim$35 × 35 mm) was prepared for each condition. The stage oscillation technique, with 10 mm linear movement, was employed to cover a large area (i.e. $\geqslant 14 \times 12\ mm^2$) for the XRD texture measurement. Indeed, this method enables analysis of more than 650 prior β grains.

2.4. EBSD measurement

The EBSD measurement was performed using a field emission gun Quanta 3D FEI scanning electron microscope operated at 20 kV and 4 nA. The instrument was equipped with a fully automated EBSD device attachment. Data acquisition and post-processing were performed using TexSEM Laboratories, Inc., software (TSL). Multiple EBSD maps were acquired using a spatial step size of 0.1 μm and 1 μm on a hexagonal grid for the martensitic and lamellar $\alpha+\beta$ microstructures, respectively. The total area covered $\sim$280,500 μm^2 for the martensitic structure. The average confidence index generally varied between 0.48 and 0.60, depending on the step size and microstructure.

2.5. Intervariant interface/boundary character distribution

A stereological procedure was employed in the current study to measure the intervariant boundary character distribution from the EBSD data, as described in detail elsewhere [32]. This procedure mainly requires a sufficient number of traces, i.e. the intersection lines between a boundary (here in two adjacent interface variants) and the surface. The traces are characterized by the lattice misorientation and orientation within the section plane. Although it is impossible to determine the orientation of the actual plane for each trace, the plane must be located in the zone of the trace. Therefore, if sufficient traces (e.g. more than 200,000 boundary traces for a hexagonal material [32]) are collected from the EBSD data, it is possible to determine the distribution of the grain boundary plane orientations. The grain boundary character distribution $\lambda(\Delta g, \mathbf{n})$ is the relative areas of distinguishable boundaries characterized by their lattice misorientation (Δg) and boundary plane orientation ($\mathbf{n}$). It is measured in multiples of a random distribution (MRD), where values >1 mean that planes were observed more frequently than expected in a random distribution.

The TSL software was initially employed to extract the intervariant boundary lines/segments to measure the intervariant interface/boundary character distribution using the stereological procedure. Briefly, a grain dilation clean-up function was first applied to all orientation maps to eliminate ambiguous data. A single orientation was then assigned to a given grain by averaging all orientation data belonging to that grain. The EBSD data were then used here to collect the required information for calculating the intervariant plane character distribution. The line traces/segments were extracted after smoothing uneven grain boundaries using the reconstruct grain boundaries function in the TSL software, using a boundary deviation limit of two pixels (i.e. 0.2 μm). There were $\sim$600,000 line traces after excluding the boundary segments of <0.3 μm. These line traces were employed to calculate the five-parameter boundary character distribution.

3. Results

The as-received microstructure was dominated by coarse α colonies (Fig. 2a). Some colonies consisted of parallel plates with similar orientation having misorientation angles in the range 0.2–2.5° (Fig. 2b). However, there were also regions where α plates were mostly fragmented into small segments, suggesting that the as-received microstructure was subjected to deformation. The α plates had an average thickness of 2.4 μm, delineated by fine β layers with a typical thickness of 0.1–0.5 μm (shown by white arrows in Fig. 2a). The XRD results also revealed the presence of the β phase in the as-received microstructure. However, it was not possible to measure the β phase texture by XRD, because it made up such a small fraction of the microstructure in the as-received condition (Fig. 3).

3.1. Microstructure and texture development through the β-to-α phase transformation

The XRD analysis of the as-quenched specimen did not reveal any β phase peaks (Fig. 3), suggesting that the coarse prior β grains, with an average size of $\sim$450 μm, were fully transformed to martensite through reheating at 1100 °C followed by ice-water quenching. The microstructure was comprised of α-martensitic laths with different orientations distributed throughout the microstructure, with an average lath thickness of $\sim$0.4 μm (Fig. 2c, d). The prior β grain boundaries are preferential sites for nucleation of martens-

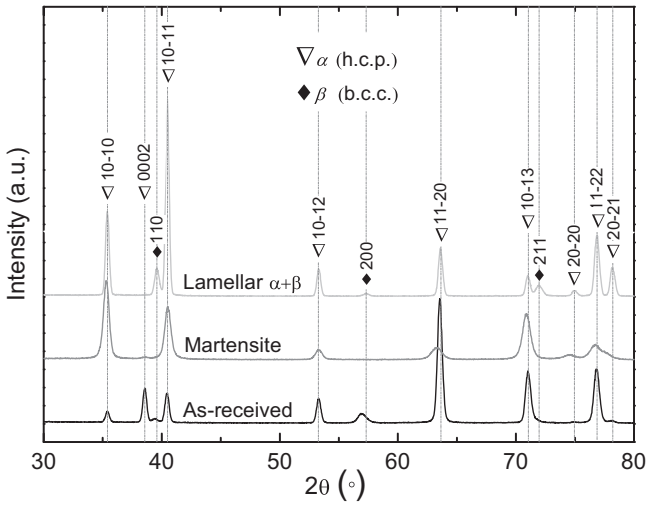

Fig. 3. XRD patterns of the Ti–6Al–4V alloy in different thermomechanical conditions: as-received, martensitic and lamellar $\alpha+\beta$ microstructures.

ite laths at an early stage of the phase transformation. It appeared that the laths nucleated on opposite sides of a given β boundary mostly had different orientations (shown by white boxes in Fig. 2d). However, there were some prior beta boundaries where martensitic variants that formed on both sides of the same part of the boundary had very close orientations (shown by the black box in Fig. 2d).

In terms of martensite lath size, two types of martensitic laths were regularly detected in the microstructure and are referred to as primary and secondary laths. The former were parallel-sided coarse laths, which stretched across the parent β grain. They were most likely formed at an early stage of the martensitic phase transformation. The latter were characterized as fine laths and largely observed between the primary coarse laths (Fig. 4). This suggests that they were formed at a later stage of the phase transformation [10]. SEM-AsB examination revealed very fine parallel lines in some of the primary coarse laths (shown by the arrows in Fig. 4). These fine features were characterized as twins. The size of the twins was in the range 20–50 nm [10], which is much smaller than the activation volume, generated through the interaction of electron beam with the specimen at 20 kV for EBSD measurement. Therefore, it would be expected that these twins would not be readily detected by the conventional EBSD measurement.

The martensitic texture revealed two relatively strong texture components in the (0002) pole figure, representing the Euler angles of $\{90°,90°,0°\}$ and $\{90°,30°,0°\}$ (Fig. 5a, b). The martensitic texture had a maximum strength of 7.8 times random (Fig. 5a, b). The main texture component was $\{90°,90°,0°\}$ with the maximum intensity of 7.8 times random, corresponding to the basal pole orientated towards the RD in the (0002) pole figure (Fig. 5a, b). The $\{90°,30°,0°\}$ texture component, with a maximum intensity of 5.5 times random, refers to basal poles rotated ~30° away from the normal direction towards the RD in the (0002) pole figure (Fig. 5a, b). This is a typical texture

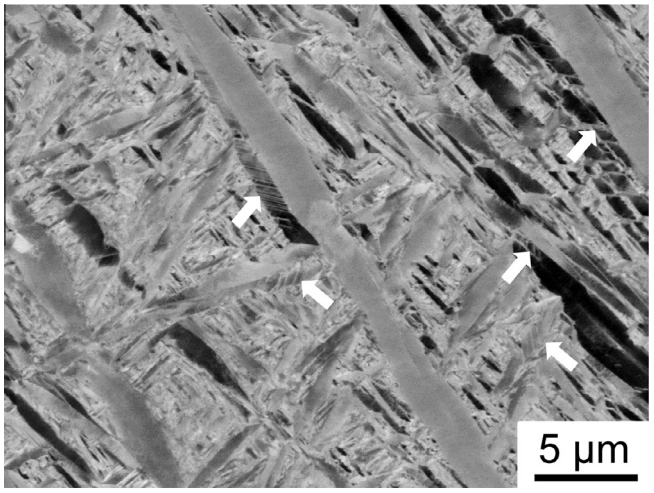

Fig. 4. AsB-SEM image of martensitic microstructure.

observed in the $\beta \rightarrow \alpha$ phase transformation of a Ti–6Al–4V alloy, taking place through a diffusional mechanism (i.e. slow cooling) [12,15], as described in detail below.

The microstructure of the slow-cooled specimen consisted of continuous films of α, with thickness of ~15 μm, decorating the prior β grain boundaries and large colonies of Widmanstätten α, nucleated mainly on the grain boundary α film (as shown by the black arrows in Fig. 2e, f). The formation of an α film on prior β grain boundaries enables measurement of the prior β grain size. The average size of the prior β grains was estimated to be ~420 μm. The average sizes of the Widmanstätten α plates and colonies were ~13 μm and ~105 μm, respectively. The Widmanstätten α plates were mostly separated by a fine β phase layer, with thickness ~1–3 μm (Fig. 2e, f). The volume fraction of the β phase was estimated by XRD to be ~8% (Fig. 3).

The α texture in the slow-cooled condition (i.e. the lamellar $\alpha + \beta$ microstructure) revealed two major orientation components at the Euler angles of $\{90°,90°,0°\}$ and $\{90°,30°,0°\}$, similar to the martensite texture (Fig. 5c, d). However, the texture strength was much higher (i.e. 13.9 times random) compared with the martensitic transformation taking place through a displacive mechanism (i.e. rapid cooling, 7.8 times random). These texture components have been observed frequently in the Ti–6Al–4V alloys transformed through slow cooling [12,15].

The β texture in the slow-cooled microstructure showed one main orientation component of $\{1\,1\,2\}\langle 1\,\bar{1}\,0\rangle$ corresponding to the Euler angles of $\{0°,33°,45°\}$ (Fig. 5e). The retained β phase in the slow-cooled sample provides a measure of the texture of parent β because of the texture memory effect [12]. Indeed, the retained β phase in the as-received microstructure can act as pre-existing nuclei during reheating from ambient to above the β transus temperature. Hence, the pre-existing β phase grows preferentially during phase transformation rather than nucleating new β grains. As a result, the β texture can be imitated from the pre-existing β orientation in the as-received microstructure, although it might be altered somewhat by grain growth.

In the current study, two different cooling rates were used to obtain the $\beta \rightarrow \alpha$ phase transformation. However, the reheating conditions (temperature and holding time) were designed so that a comparable prior β grain size (i.e. ~450 μm for martensite and ~420 μm for lamellar $\alpha + \beta$ microstructure) was obtained before the phase transformation for both cooling paths. Therefore, the extent of β grain growth was expected to be the same for both heat treatment conditions. The β texture, measured from the slow-cooled microstructure, should also provide a good representation of the parent β texture prior to the martensitic phase transformation.

3.2. Intervariant crystallographic plane distribution in the martensitic phase transformation

Theoretically, the transformation of the parent β phase (i.e. bcc) to the α phase with the hexagonal crystal structure

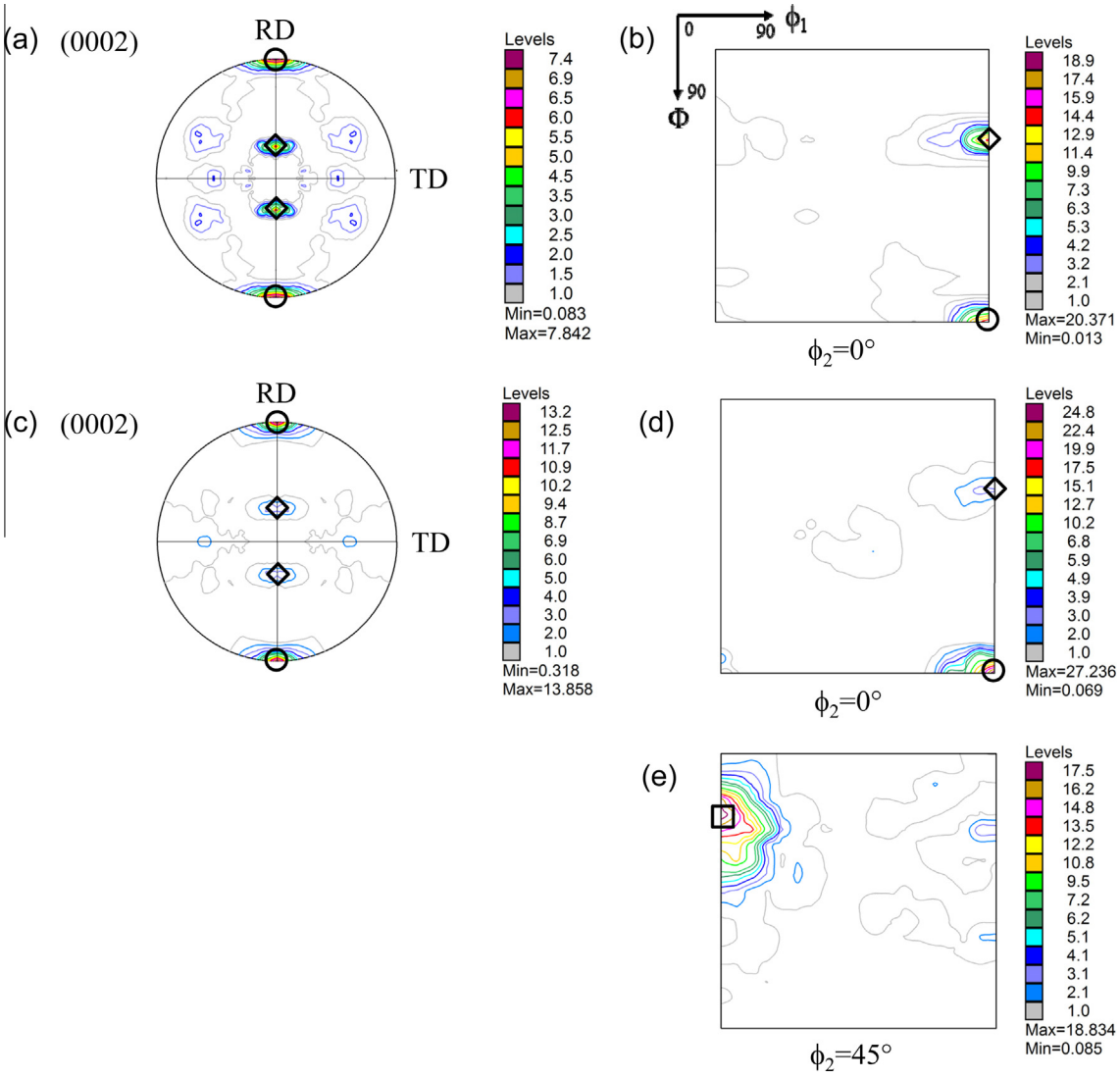

Fig. 5. The pole figure and ODF section of $\varphi_2 = 0°$ for α texture of the Ti–6Al–4V alloy at different phase transformation conditions: (a, b) martensitic and (c, d) lamellar α + β microstructures. (e) The ODF section of $\varphi_2 = 45°$ for the β in the lamellar α + β microstructure. RD and TD are rolling and transverse directions, respectively. ○ {90°, 90°, 0°}; ◇ {90°, 30°, 0°}; □ {0°, 33°, 45°}.

(e.g. martensitic phase transformation) follows the Burgers orientation relationship, where it is assumed that the close-packed plane of the parent β (i.e. {1 1 0}) would be parallel to the close-packed plane of the transformed product (i.e. α, $\{1\,1\,0\}_\beta \parallel (0\,0\,0\,1)_\alpha$ and $\langle 1\,1\,\bar{1}\rangle_\beta \parallel \langle 1\,1\,\bar{2}\,0\rangle_\alpha$) during the phase transformation (Fig. 1). As a result, each prior β grain can transform up to 12 different orientation variants of α, as listed in Table 1. By comparing all 12 variants, 11 misorientation angle/axis sets can be computed (Table 1). Some of these intervariant interfaces are identical as a result of the crystal symmetry (e.g. V_1–V_2 and V_1–V_3), as reported earlier by others [9]. Hence, the comparison of all 12 variants in the case of the Burgers orientation relationship reduces to only five independent misorientations. Consequently, the misorientation angle distribution of martensite was quantitatively different from that of the random distribution (see Fig. 6). The misorientation angle distribution showed four distinct peaks in the angular ranges 8–12°, 55–65° (two peaks) and 88–92°. These misorientation ranges were closely correlated to the possible intervariant misorientation angles for the Burgers orientation relationship (Fig. 6 and Table 1). Similarly, the axes for each of these misorientation ranges corresponded closely to the theoretical axes computed for the Burgers orientation relationship (Fig. 6 and Table 1). The greatest peak at ~63° was close to the $[\overline{10}\,5\,5\,\overline{3}]$ misorientation axis. The peak at the misorientation angle range of 55–62° was associated with both the $[1\,1\,\overline{2}\,0]$ and $[\overline{1.377}\,\overline{1}\,2.377\,0.359]$ misorientation axes. The peaks at the misorientation angles of 8–12° and 88–92° corresponded to the misorientation axes of [0 0 0 1] and $[1\,\overline{2.38}\,1.38\,0]$, respectively (Fig. 6).

Fig. 7 shows the total population fraction of intervariant interfaces related to the Burgers orientation relationship. It appeared that most intervariant boundary fractions belonged to the laths with misorientation angles/axes of 63.26°/$[\overline{10}\,5\,5\,\overline{3}]$ and 60°/$[1\,1\,\overline{2}\,0]$, with ~0.38 and ~0.3 of

Table 1
Twelve possible variants generated by the martensitic β → α phase transformation through the Burgers orientation relationship [9].

Variant	Plane parallel	Direction parallel	Rotation angle/axis from V1
V1	$(1\,\bar{1}\,0)_\beta \parallel (0\,0\,0\,1)_\alpha$	$[1\,1\,1]_\beta \parallel [1\,1\,\bar{2}\,0]_\alpha$	–
V2	$(1\,0\,\bar{1})_\beta \parallel (0\,0\,0\,1)_\alpha$	$[1\,1\,1]_\beta \parallel [1\,1\,\bar{2}\,0]_\alpha$	60°/[1 1 $\bar{2}$ 0]
V3	$(0\,1\,\bar{1})_\beta \parallel (0\,0\,0\,1)_\alpha$	$[1\,1\,1]_\beta \parallel [1\,1\,\bar{2}\,0]_\alpha$	60°/[1 1 $\bar{2}$ 0]
V4	$(1\,1\,0)_\beta \parallel (0\,0\,0\,1)_\alpha$	$[\bar{1}\,1\,1]_\beta \parallel [1\,1\,\bar{2}\,0]_\alpha$	90°/[1 $\overline{2.38}$ 1.38 0]
V5	$(1\,0\,1)_\beta \parallel (0\,0\,0\,1)_\alpha$	$[\bar{1}\,1\,1]_\beta \parallel [1\,1\,\bar{2}\,0]_\alpha$	63.26°/[$\bar{1}$0 5 5 $\bar{3}$]
V6	$(0\,1\,\bar{1})_\beta \parallel (0\,0\,0\,1)_\alpha$	$[\bar{1}\,1\,1]_\beta \parallel [1\,1\,\bar{2}\,0]_\alpha$	60.83°/[$\overline{1.377}$ $\bar{1}$ 2.377 0.359]
V7	$(1\,1\,0)_\beta \parallel (0\,0\,0\,1)_\alpha$	$[1\,\bar{1}\,1]_\beta \parallel [1\,1\,\bar{2}\,0]_\alpha$	90°/[1 $\overline{2.38}$ 1.38 0]
V8	$(1\,0\,\bar{1})_\beta \parallel (0\,0\,0\,1)_\alpha$	$[1\,\bar{1}\,1]_\beta \parallel [1\,1\,\bar{2}\,0]_\alpha$	60.83°/[$\overline{1.377}$ $\bar{1}$ 2.377 0.359]
V9	$(0\,1\,1)_\beta \parallel (0\,0\,0\,1)_\alpha$	$[1\,\bar{1}\,1]_\beta \parallel [1\,1\,\bar{2}\,0]_\alpha$	63.26°/[$\bar{1}$0 5 5 $\bar{3}$]
V10	$(1\,\bar{1}\,0)_\beta \parallel (0\,0\,0\,1)_\alpha$	$[1\,1\,\bar{1}]_\beta \parallel [1\,1\,\bar{2}\,0]_\alpha$	10.53°/[0 0 0 1]
V11	$(1\,0\,1)_\beta \parallel (0\,0\,0\,1)_\alpha$	$[1\,1\,\bar{1}]_\beta \parallel [1\,1\,\bar{2}\,0]_\alpha$	60.83°/[$\overline{1.377}$ $\bar{1}$ 2.377 0.359]
V12	$(0\,1\,1)_\beta \parallel (0\,0\,0\,1)_\alpha$	$[1\,1\,\bar{1}]_\beta \parallel [1\,1\,\bar{2}\,0]_\alpha$	60.83°/[$\overline{1.377}$ $\bar{1}$ 2.377 0.359]

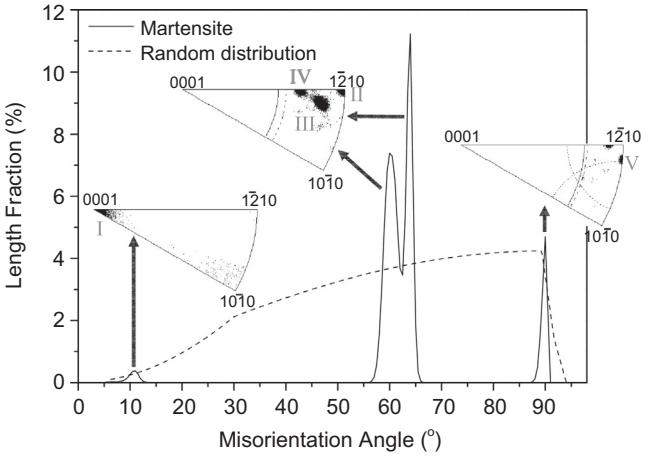

Fig. 6. The dashed line represents the random distribution of the misorientation angle. The black line is the misorientation angle distribution of martensite along with misorientation axes for specific disorientation angles associated with the Burgers orientation relationship: (i.e. I = 10.53°/[0 0 0 1], II = 60°/[1 1 $\bar{2}$ 0], III = 60.83°/[$\overline{1.377}$ $\bar{1}$ 2.377 0.359], IV = 63.26°/[$\bar{1}$0 5 5 $\bar{3}$], and V = 90°/[1 $\overline{2.38}$ 1.38 0].

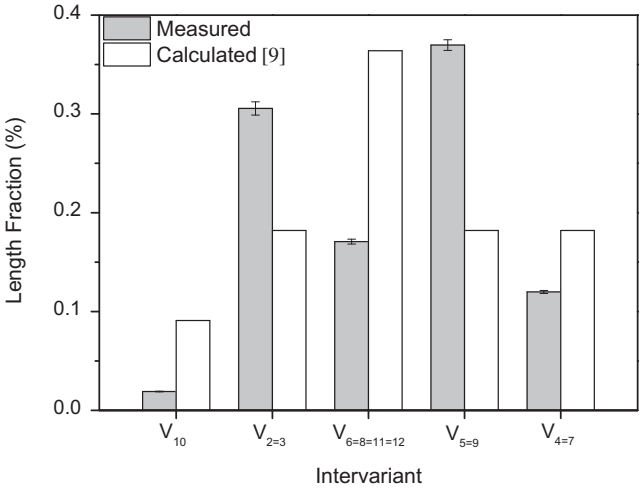

Fig. 7. The length fraction of total population of interfaces that belong to the Burgers orientation relationship, comparing intervariant interfaces between V1 and V*i* (*i* = 2–12) for the martensite: (a) measured and (b) theoretically calculated fractions, assuming that all variants are formed with equal statistical probability during martensitic phase transformation [9]. Because of symmetry, there are only five independent intervariant interfaces, and the = sign shows equivalent intervariant interfaces.

total population, respectively. The lowest population was related to the 10.53°/[0 0 0 1] misorientation, covering <0.02 of the total population, where this is the interface that forms as a result of the intersection of two distinct crystallographic laths bounded with a given β phase habit plane. In general, the frequency with which the different variants were adopted closely correlated with the misorientation angle distribution (Figs. 6 and 7).

The relative area distribution of boundary planes λ(*n*) is plotted in stereographic projection to investigate the distribution of intervariant interface/boundary planes in the crystal reference frame (see Fig. 8). Here, the basal orientation (i.e. (0 0 0 1) plane) was located in the center of the stereogram, and the prismatic orientations (e.g. {1 0 $\bar{1}$ 0} and {1 1 $\bar{2}$ 0} planes) were positioned at the stereogram circumference. The stereological calculation of the boundary/interface character distribution assumes that the grain pairs are uniformly distributed in orientation space. In other words, each group of bicrystals in the data set with identical misorientation must be randomly orientated. However, where the sample is textured, similar to the present case, this assumption cannot be employed. In the current study, the texture-induced bias in the distribution of observed bicrystal orientations was first removed to calculate the grain boundary character distribution. In this approach, all observations related to a specific misorientation type were weighted inversely according to their frequency of appearance in a given range of orientation space. This procedure, indeed, recovers the desired random distribution of orientations for each bicrystal type and removes texture-induced bias in the stereological calculation. The analysis was carried out at 9 bins per 90° level of discretization, which offers ~10° resolution in the current study. At this resolution, 97% of the bins contained at least 10 observations.

The intervariant plane distribution of martensite independent of misorientation, λ(**n**), where **n** is the normal to the intervariant boundary, was anisotropic. It displayed a maximum value of 1.63 MRD at the {1 0 $\bar{1}$ 0} orientation that spread towards the {4 $\bar{1}$ $\bar{3}$ 0} planes (Fig. 8). This sug-

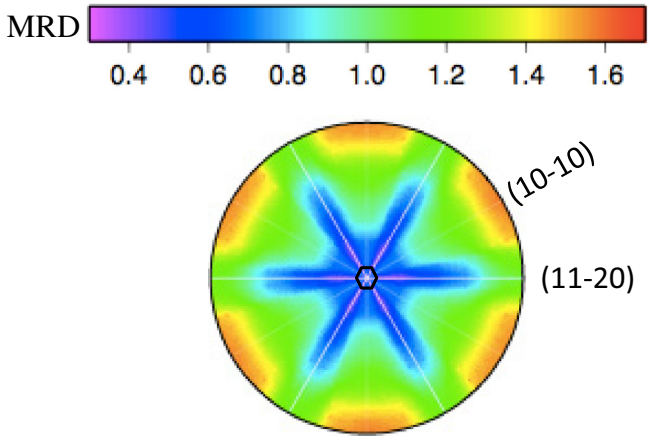

Fig. 8. Distribution of intervariant boundary/interface planes for all misorientations in martensitic microstructure. MRD represents multiples of random distribution. ⬡ is the position of (0001) plane.

gests that most intervariant interfaces were terminated on prismatic planes (i.e. {*hki*0}) ranging mostly from the {1 0 $\bar{1}$ 0} and {4 $\bar{1}$ $\bar{3}$ 0} planes, as the population of these planes was 63% greater than expected in a random distribution. The minimum of the distribution was centered at the (0001) basal plane with 0.37 MRD (Fig. 8). The distribution at the position of {1 1 $\bar{2}$ 0} prism planes was moderately high, having a value of ~1.2 MRD.

The intervariant plane distributions were also plotted for specific misorientation types associated with the Burgers orientation relationship, using five macroscopic boundary parameters (Fig. 9). Overall, significant differences were observed in the distribution of intervariant planes as a function of misorientation. The distribution of intervariant planes at 10.53°/[0001] had multiple maxima, mostly along the zone of tilt boundaries (i.e. the great circle perpendicular to the [0001] axis). The maxima were spread along the positions of the {1 0 $\bar{1}$ 0} and {1 1 $\bar{2}$ 0} prism planes with ~0.9 MRD (Fig. 9a). In other words, the normals to these planes were perpendicular to the misorientation axis of [0001], indicating that the boundary planes had a tilt character. Here, when a lath/crystal is, for example, terminated by the {1 0 $\bar{1}$ 0} plane, the geometrically required parallel plane complement is a crystal rotated by 10.53° around the [0001] axis, which would be close to the (20 9 $\overline{29}$ 0) plane. Therefore, the complementary planes perpendicular to the [0001] axis were not the same, suggesting that they had an asymmetric tilt character.

At a misorientation of 60°/[1 1 $\bar{2}$ 0], the intervariant planes distribution showed a pronounced peak, with a maximum of ~372 MRD at a position close to the ($\bar{1}$ 0 1 1) pyramidal plane. This boundary, in fact, had a symmetric tilt character as the plane normal is perpendicular to the misorientation axis (Fig. 9b). The distribution of intervariant planes at 60.83°/[$\overline{1.377}$ $\bar{1}$ 2.377 0.359] had a moderate maximum of ~26.5 MRD between the (0 $\bar{1}$ 1 0) and ($\bar{1}$ $\bar{1}$ 2 0) planes (i.e. close to (4 $\bar{1}$ $\bar{3}$ 0) plane; Fig. 9c). Similar to the misorientation angle distribution, a very strong peak was observed in the intervariant planes distribution at 63.26°/[$\overline{10}$ 5 5 $\bar{3}$]. The maximum was ~716 MRD at a position near the (4 $\bar{1}$ $\bar{3}$ 0) plane (Fig. 9d). At the misorientation of 90°/[1 $\overline{2.38}$ 1.38 0], a moderate single peak was revealed in the intervariant planes distribution with ~42 MRD, close to (1 0 $\bar{1}$ 1) pyramidal plane (Fig. 9e). Apart from 10.53°/[0001] and 60°/[1 1 $\bar{2}$ 0], the intervariant plane distributions of the other misorientations did not reveal any twist or tilt character (Fig. 9). Though, it is possible they have tilt or twist character in some other representation [34].

4. Discussion

4.1. Variant selection during the β-to-α phase transformation

The texture developed through the martensitic phase transformation (i.e. rapid cooling) is qualitatively similar

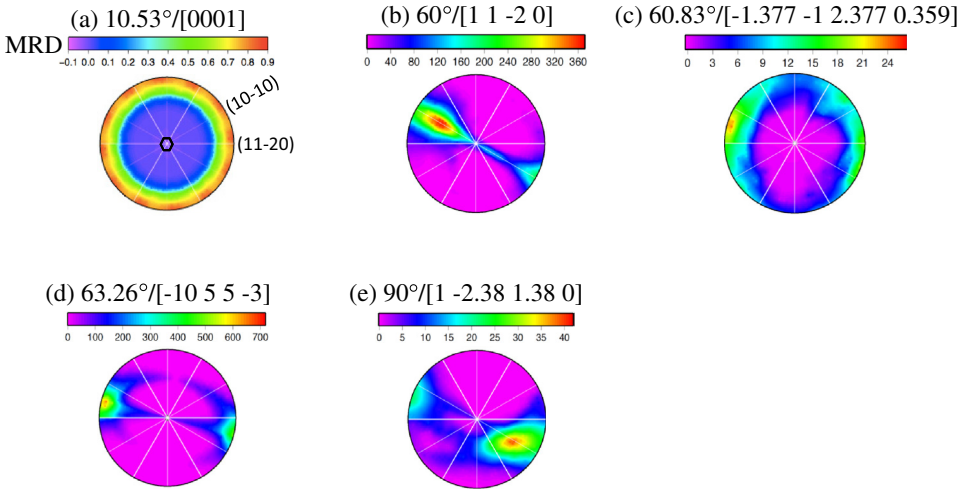

Fig. 9. Distribution of intervariant interface/boundary planes for different misorientations associated with the Burgers orientation relationship. MRD and ⬡ in (a) represent multiples of random distribution and the position of (0001) plane, respectively.

to the β → α phase transformation texture that results from slow cooling (i.e. diffusional mechanism), where the two main texture components with the Euler angles of (90°, 90°, 0°) and (90°, 30°, 0°) are present in the (0 0 0 2) pole figure (Fig. 5a–d). Here, the main difference is the overall texture strength, where the slow-cooling condition reveals greater texture strength (i.e. 13.9 times random) compared with the martensitic structure (i.e. 7.8 times random, Fig. 5a–d). In Ti alloys, the phase transformation texture characteristics are attributed mainly to the presence of a strong crystallographic variant selection mechanism governed by the Burgers orientation relationship during the β → α phase transformation [11,12,15], where under specific circumstances certain orientations/variants are formed more frequently than others.

It is well demonstrated that the crystallographic variant selection significantly depends on the *c*-axis alignment of α variants initially nucleated on both sides of a β grain boundary. The formation of the (90°, 30°, 0°) component, for example, is a result of the nucleation of a given α variant on both sides of β grain boundaries terminated by {1 1 0} planes [11,12,15]. On reheating, the inverse α → β phase transformation produces six distinct crystallographic β variants from a given α variant/grain. These β variants share common (1 1 0) planes with a twin relationship, as shown by others in pure Ti [14,35]. Interestingly, the (1 1 0) plane is the close-packed and minimum energy plane in the bcc crystal structure [36]. In other words, the inverse α → β phase transformation promotes the low-energy (1 1 0) planes, which can enhance the formation of the (90°, 30°, 0°) component as a result of the preferential nucleation of a given α variant on both sides of β grain boundaries with a common (1 1 0) normal [11,12,15].

There are different factors influencing the extent of crystallographic variant selection during the β → α phase transformation in Ti alloys, such as alloy composition [15,37], prior β grain size [14,15], initial β texture, and phase transformation path (i.e. cooling rate) [37]. Alloys with different additions (e.g. β stabilizers) can alter the phase transformation product characteristics [37]. As the composition of the alloy is the same for both the martensite (i.e. rapid cooling) and lamellar α + β (i.e. slow cooling) microstructures in the current study, the effect of composition on the variant selection mechanism can be ruled out. The coarsening of the parent β grains also enhances the crystallographic variant selection resulting a strong (90°, 30°, 0°) component in the phase transformation texture [15]. Interestingly, the β grain size prior to the martensitic transformation is ~450 μm (Fig. 2c, d), which is comparable with the β grain size (i.e. 420 μm) that transformed to the lamellar α + β microstructure on slow cooling (Fig. 2e, f). This suggests that the observed phase transformation texture in the martensitic structure is related mostly to either the β texture and/or phase transformation path (i.e. cooling rate).

In the current study, the reheating schedule was the same for both the martensitic and lamellar α + β microstructures. Therefore, it would be expected that the texture of β formed on reheating would be similar before the β → α transformation for both heat treatment conditions (i.e. cooling rates; Fig. 5e). The initial β texture in the current study is very similar to the earlier work [14], where they used the measured β texture to calculate the α texture assuming no variant selection taking place during the β → α phase transformation [14]. Interestingly, the calculated α texture is very similar to the martensite texture formed in the current study, though it shows slightly stronger texture strength (~10 times random) than the present martensite (i.e. 7.8 random times). This suggests that the reduction in the texture strength is attributed mainly to the phase transformation path (i.e. martensitic transformation/cooling rate) through weakening of the crystallographic variant selection.

The nucleation of a preferred α-variant on a β grain boundary reduces the boundary energy and the strain energy induced during the β → α phase transformation [17,18]. The phase transformation driving force is small at a high transformation temperature, which is what happens during slow cooling. This results in the selection of a specific variant to nucleate preferentially on a given β grain boundary. The differences in the activation energies for the nucleation of different α variants reduces with an increase in the cooling rate (i.e. a decrease in the transformation temperature). In addition, the β phase strength enhances with a decrease in the phase transformation temperature (e.g. rapid cooling), promoting different variant formation to self-accommodate the transformation strain. In other words, the martensitic transformation, taking place as a result of rapid cooling, significantly weakens the crystallographic variant selection during the β → α phase transformation. Similar observations were reported for the variant selection mechanism in the bainitic phase transformation in steels [17,18]. Consequently, the formation of multiple variants is frequently observed on either side of a given prior β boundary in the martensitic structure (shown by the white boxes in Fig. 2d), which reduces the strength of the texture (i.e. weakening the variant selection). Occasionally, α variants with a similar orientation are found on both sides of a given β grain boundary in the martensitic microstructure (shown by the black box in Fig. 2d), which can contribute in the formation of the (90°, 30°, 0°) component in the martensitic texture.

4.2. Intervariant crystallographic plane distribution in the martensitic phase transformation

The current intervariant plane distribution analysis clearly demonstrates that only five misorientation types frequently result from the martensitic phase transformation. These misorientations are all associated with the Burgers orientation relationship. However, they have significantly different frequencies and are terminated by distinct crystallographic planes.

The highest intervariant boundary fractions between adjacent laths belong to misorientations of 63.26°/

[$\overline{10}$ 5 5 $\overline{3}$] and 60°/[1 1 $\overline{2}$ 0], making up ~0.38 and ~0.3 of the total population, respectively. In other words, more than two-thirds of all interfaces have this character. This is much higher than would be expected if all 12 variants were formed with equal statistical probability (Fig. 7). Similar observations were reported in martensitic microstructures formed in pure Ti [9], although they had different populations, which may be due to the composition. In the prior work on pure Ti, it was demonstrated that specific variant clustering arrangements take place during the martensitic transformation to self-accommodate the shape strains produced through the displacive transformation. The variant clusters promote mainly the formation of two intervariant misorientations of 63.26°/[$\overline{10}$ 5 5 $\overline{3}$] and 60°/[1 1 $\overline{2}$ 0]. The other three intervariant misorientations (i.e. 10.53°/[0 0 0 1], 60.83°/[$\overline{1.377}$ $\overline{1}$ 2.377 0.359] and 90°/[1 $\overline{2.38}$ 1.38 0]) are, indeed, the result of impingement of these variant clusters [9].

The grain boundary population has, on average, an inverse relationship with the relative grain boundary energy in microstructures produced by normal grain growth, as demonstrated by various simulations [38–40] and experiments for materials with different crystal structures [24,41,42,36,43]. In other words, the most frequently observed boundaries appear to have the lowest energies, and the least populated boundaries, in contrast, have high energies [24,41,42,36,43]. Here, the interplanar spacing of planes (i.e. d_{hkl}) can be used as a measure to compare the relative grain boundary energy for different planes [31,44]. Generally, the interfaces consisted of planes with large interplanar spacings, which have lower energies as they are relatively flat, and two smooth facets match better than two rough ones. In other words, improved fit at the interface increases the attractive forces across the boundary and reduces the repulsion, which consequently lowers the boundary energy [31,44]. The interplanar spacings of some common planes observed in the intervariant interface distribution produced by the martensitic phase transformation are summarized in Table 2. Here, it appears there is no direct relationship between the interplanar spacings with the populations. For example, the most frequently observed plane of (4 $\overline{1}$ $\overline{3}$ 0) has the minimum interplanar spacing of 0.70 Å, while the (0 0 0 1) plane, with an interplanar spacing of 4.7 Å, has the smallest population in the distribution (Fig. 9 and Table 2). In other words, the planes with the highest energy have the greater population and vice versa, suggesting that the interface distribution produced by the martensitic phase transformation is not inversely related to the grain boundary energy.

Interestingly, the ($\overline{1}$ 0 1 1) plane, which has the second highest population (Fig. 9b), has the minimum energy among the [1 $\overline{2}$ 1 0] symmetric grain boundaries, as measured by molecular dynamic simulation [45]. This plane, indeed, corresponds to the $\{1\,0\,\overline{1}\,1\}\langle\overline{1}\,0\,1\,2\rangle$ twin boundary in the hexagonal crystal structure (i.e. 61.35°/[1 $\overline{2}$ 1 0]) [9,10]. The calculated energy of [1 $\overline{2}$ 1 0] symmetric grain boundaries as a function of misorientation also reveals three other cusps at the positions of twin boundaries of 31.39°/[$\overline{1}$ 0 1 3], 42.47°/[$\overline{1}$ 0 1 2], and 74.7°/[$\overline{2}$ 0 2 1] [45]. Interestingly, the current result does not show the presence of any of the other three misorientation angles (31.39°, 42.47° and 74.7°) in the misorientation angle distribution (Fig. 6). This suggests that the presence of a high fraction of ($\overline{1}$ 0 1 1) in the current study is not specifically due to the low-energy configuration, as suggested earlier [9,10].

Table 2
The interplanar spacings (d_{hkl}) for different measured intervariant planes.

Plane	Interplanar spacings (Å)
(1 0 -1 0)	2.54
(1 1 -2 0)	1.47
(-1 0 1 1)*	0.37 or 1.86
(4 -1 -3 0)	0.70
(0 0 0 1)	4.7

* For (-1 0 1 1) plane, the structure factor was taken into account as the plane passing through an additional atom [48].

The current results also differ from the grain boundary plane distribution observed in WC at a steady-state condition, where the boundaries are expected to have the minimum energy configuration [30,31]. The most common planes observed in WC were $\{1\,0\,\overline{1}\,0\}$, (0 0 0 1) and $\{1\,1\,\overline{2}\,0\}$, revealing low-energy interfaces [30,31]. One could argue that the difference between the boundary plane distribution in WC and the current result arises from the difference in the c/a ratio of WC (i.e. 0.976 [31]) compared with Ti–6Al–4V alloy (i.e. 1.598 [35]) or its multi-atomic basis. Therefore, the observation that low-energy interfaces are qualitatively similar for a given cubic crystal structure in both experiments [42,43] and modeling [45–47] does not necessarily apply to a comparison between Ti–6Al–4V alloy and WC.

Recently, the grain boundary plane distribution of a Ti–6Al–4V alloy with two different heat treatment conditions was examined for a limited number of misorientations [29]. The misorientation angle distribution was qualitatively similar to the martensitic structure, although the peak intensities were much lower. Interestingly, the misorientations examined revealed a plane character similar to that of martensite. However, the population was much lower than in the current study, especially for the sample subjected to annealing. These distributions were attributed mostly to the β → α phase transformation rather than low-energy configuration [29]. This is not surprising, as the processing path can greatly influence the grain boundary plane distribution [28], even overwhelming the effect of the grain boundary energy [24,41,42,36,43].

During the martensitic shear phase transformation in Ti alloys, a strong crystallographic relationship is present between the parent (i.e. β) and the product (i.e. α lath martensite), which follows the Burgers orientation relationship. According to the ideal Burgers orientation relationship, the close-packed planes of the α lath martensite (i.e. basal plane) match the close-packed planes of adjacent β (i.e.

$\{1\,1\,0\}_\beta \parallel (0\,0\,0\,1)_\alpha$; Fig. 1). Considering constraints associated with the shear transformation and the hexagonal crystal structure, two adjacent martensite laths would be expected to, most likely, impinge on prismatic $\{hki0\}$ planes after the completion of the phase transformation (i.e. growth). This strongly agrees with the current observation, where the distribution of intervariant planes for all misorientations reveals more frequent prism planes $\{hki0\}$ than any other plane orientations (Fig. 8). As an example, the frequency of $\{1\,0\,\bar{1}\,0\}$ prism planes is more than 5.5 times greater than that of the (0001) basal plane, suggesting relatively high anisotropy in the distribution of intervariant planes in the martensitic microstructure (Fig. 8). Interestingly, the population of planes is not inversely correlated with energy, as the interplanar spacing of the (0001) plane (i.e. 4.7 Å) is much greater than that of $\{1\,0\,\bar{1}\,0\}$ planes (i.e. 2.54 Å; Fig. 8 and Table 2). In other words, the distribution of intervariant interfaces in martensite is governed mostly by the phase transformation and crystal structure constraints rather than low-energy grain boundary configurations.

5. Conclusions

In the current study, the effect of the phase transformation mechanism on texture development was investigated in a Ti–6Al–4V alloy. The crystallographic texture characteristics were relatively similar for microstructures formed by displacive (i.e. martensite) and diffusional (i.e. $\alpha+\beta$ microstructure) phase transformations, revealing two main texture components with Euler angles of $(90°, 90°, 0°)$ and $(90°, 30°, 0°)$. Nevertheless, the martensitic transformation considerably reduced the overall α texture strength compared with the $\alpha+\beta$ microstructure. The crystallographic variant selection was, in fact, weakened through the martensitic transformation. The ability to measure all five independent crystallographic grain boundary parameters in the current study enabled the present authors to comprehensively survey the intervariant boundary distribution in martensite transformed in a Ti–6Al–4V alloy. The misorientation angle distribution of the martensitic structure presented only five misorientations associated with the Burgers orientation relationship. The five-parameter boundary analysis of the intervariant interfaces also revealed very strong plane texture, mostly terminated on prismatic planes, $\{hki0\}$. The 63.26°/$[\bar{1}0\,5\,5\,\bar{3}]$ and 60°/$[1\,1\,\bar{2}\,0]$ had the highest intervariant boundary populations with a total fraction of ~0.68, which was much greater than expected for a random distribution of all variants (i.e. ~0.36 [9]). The 63.26°/$[\bar{1}0\,5\,5\,\bar{3}]$ and 60°/$[1\,1\,\bar{2}\,0]$ misorientations were terminated on $(4\,\bar{1}\,\bar{3}\,0)$ and $(\bar{1}\,0\,1\,1)$ planes, respectively. The intervariant crystallographic plane distribution in martensite was determined by the crystallographic constraints associated with the phase transformation and not by the relative energies of the interfaces.

Acknowledgments

The work at Deakin University was supported through grants provided by the Australian Research Council. The authors thank Professor Peter Hodgson for his assistance in this work. The work at Carnegie Mellon University was supported by the Office of Naval Research under Grant N00014-11-1-0678.

References

[1] Burgers WG. Physica 1934;1:561–86.
[2] Vanginneken AJJ, Burgers WG. Acta Crystallogr 1952;5:548–89.
[3] Romero J, Preuss M, Quinta da Fonseca J. Acta Mater 2009;57:5501–11.
[4] Hutchinson B, Ryde L, Bate PS. Mater Sci Forum 2005;495–497:1141–50.
[5] Inoue H, Fukushima S, Inakazu N. Mater Trans JIM 1992;33:129–37.
[6] Yoshinaga N, Ushioda K, Itami A, Akisue O. ISIJ Int 1994;34:33–42.
[7] Gong W, Tomota Y, Adachi Y, Paradowska AM, Kelleher JF, Zhang SY. Acta Mater 2013;61:4142–54.
[8] Vogel SC, Bhattacharyya D, Viswanathan GB, Williams DJ. Mater Sci Forum 2005;495–497:681–6.
[9] Wang SC, Aindow M, Starink MJ. Acta Mater 2003;51:2485–503.
[10] Srivastava D, Madangopal K, Banarjee S, Ranganathan S. Acta Metall Mater 1993;41:3445–54.
[11] Bhattacharyya D, Viswanathan GB, Denkenberger R, Furrer D, Fraser HL. Acta Mater 2003;51:4679–91.
[12] Stanford N, Bate PS. Acta Mater 2004;52:5215–24.
[13] Humbert M, Germain L, Gey N, Bocher P, Jahazi M. Mater Sci Eng A 2006;430:157–64.
[14] Cayron C. Scr Mater 2008;59:570–3.
[15] Obasi GC, Birosca S, Quinta da Fonseca J, Preuss M. Acta Mater 2012;60:1048–58.
[16] Gey N, Humbert M. Acta Mater 2002;50:277–87.
[17] Beladi H, Adachi Y, Timokhina I, Hodgson PD. Scr Mater 2009;60:455–8.
[18] Furuhara T, Kawata H, Morito S, Maki T. Mater Sci Eng A 2006;431:228.
[19] Gaunt P, Christian JW. Acta Metall 1959;7:534–43.
[20] Banerjee S, Krishnan R. Acta Metall 1971;19:1317–26.
[21] Knowles KM, Smith DA. Acta Metall 1981;29:1445–66.
[22] Saylor DM, El Dasher BS, Sano T, Rohrer GS. J Am Ceram Soc 2004;87:670.
[23] Saylor DM, El Dasher BS, Pang Y, Miller HM, Wynblatt P, Rollett AD, et al. J Am Ceram Soc 2004;87:724.
[24] Saylor DM, Morawiec A, Rohrer GS. Acta Mater 2003;51:3675.
[25] Bennett TA, Kim CS, Rohrer GS, Rollett AD. Mater Sci Forum 2004;467–470:1057.
[26] Saylor DM, El Dasher BS, Rollett AD, Rohrer GS. Acta Mater 2004;52:3649.
[27] Beladi H, Rohrer GS. Metall Mater Trans A 2013;44:115.
[28] Beladi H, Rohrer GS, Rollett AD, Tari V, Hodgson PD. Acta Mater 2014:86–98.
[29] Randle V, Rohrer GS, Hu Y. Scr Mater 2008;58:183.
[30] Kim CS, Massa TR, Rohrer GS. J Am Ceram Soc 2008;91:996–1001.
[31] Kim CS, Rohrer GS. Interface Sci 2004;12:19–27.
[32] Rohrer GS, Saylor DM, El Dasher B, Adams BL, Rollett AD, Wynblatt P. Z Metallkd 2004;95:197.
[33] Hilditch T, Beladi H, Hodgson P, Stanford N. Mater Sci Eng A 2012;534:288.
[34] Glowinski K, Morawiec A. J Mater Sci 2014;49:3936–42.
[35] Lonardelli I, Gey N, Wenk HR, Humbert M, Vogel SC, Lutterotti L. Acta Mater 2007;55:5718–27.

[36] Beladi H, Rohrer GS. Acta Mater 2013;61:1404–12.
[37] Banerjee D, Pilchak A, Williams JC. Mater Sci Forum 2012;710:66–84.
[38] Gruber J, George DC, Kuprat AP, Rohrer GS, Rollett AD. Scr Mater 2005;53:351.
[39] Rohrer GS, Gruber J, Rollett AD. In: Rollett AD, editor. Ceramic transactions of applications of texture analysis, vol. 201. Hoboken, NJ: John Wiley; 2009. p. 343–54.
[40] Gruber J, Rohrer GS, Rollett AD. Acta Mater 2010;58:14.
[41] Dillon SJ, Rohrer GS. J Am Ceram Soc 2009;92:1580.
[42] Li J, Dillon SJ, Rohrer GS. Acta Mater 2009;57:4304.
[43] Beladi H, Nuhfer NT, Rohrer GS. Acta Mater 2014;70:281–9.
[44] Wolf D. J Mater Res 1990;5:1708.
[45] Wang J, Beyerlein IJ. Model Simul Mater Sci Eng 2012;20:1.
[46] Wang J, Beyerlein IJ. Metall Trans A 2012;43:3556–69.
[47] Tschopp MA, Spearot DE, Mcdowell DL. In: Hirth JP, editor. Dislocations in solids. Amsterdam: Elsevier; 2008. p. 43–97.
[48] Fan Q. Appl Crystallogr 2012;45:1303–8.